RSC Advances

PAPER

View Article Online
View Journal | View Issue



Cite this: *RSC Adv.*, 2018, **8**, 31835

# Thermally stable $La_2LiSbO_6:Mn^{4+},Mg^{2+}$ far-red emitting phosphors with over 90% internal quantum efficiency for plant growth LEDs

Liangling Sun, Balaji Devakumar, Jia Liang, Bin Li, Shaoying Wang, Qi Sun, Heng Guo and Xiaoyong Huang *

Received 31st July 2018
Accepted 5th September 2018

DOI: 10.1039/c8ra06435k

rsc.li/rsc-advances

In this paper, we reported on the high-efficiency and thermally-stable $La_2LiSbO_6:Mn^{4+},Mg^{2+}$ (LLS:$Mn^{4+}$,$Mg^{2+}$) far-red emitting phosphors. Under 338 nm excitation, the composition-optimized LLS:0.3%$Mn^{4+}$,1.6%$Mg^{2+}$ phosphors which were made up of [$SbO_6$], [$LiO_6$], and [$LaO_8$] polyhedrons, showed intense far-red emissions peaking at 712 nm ($^2E_g \rightarrow {}^4A_{2g}$ transition) with internal quantum efficiency as high as 92%. The LLS:0.3%$Mn^{4+}$,1.6%$Mg^{2+}$ phosphors also exhibited high thermal stability, and the emission intensity at 423 K only reduced by 42% compared with its initial value at 303 K. The far-red light-emitting device has also been made by using the LLS:0.3%$Mn^{4+}$,1.6%$Mg^{2+}$ phosphors and a 365 nm emitting InGaN chip, which can emit far-red light that is visible to the naked eye. Importantly, the emission spectrum of the LLS:0.3%$Mn^{4+}$,1.6%$Mg^{2+}$ phosphors can match well with the absorption spectrum of phytochrome $P_{FR}$, indicating the potential of these phosphors to be used in plant growth light-emitting diodes.

## Introduction

With the development of the economies of all countries in the world, environmental and energy issues have received increasing attention.[1–7] The use of commercial greenhouses has grown rapidly in recent years to obtain green grains and high-quality vegetables.[8,9] Light plays an important role in plant growth, because it can affect the growth rhythm of natural plants, such as delaying the plant blooming time or promoting plant blooming ahead of schedule.[10] Phytochrome $P_R$ and $P_{FR}$ can influence the plant blooming time by converting to each other; $P_R$ needs more red light peaking at 660 nm to switch to the $P_{FR}$ biologically active state, and $P_{FR}$ captures more far-red light peaking at about 730 nm to convert to the $P_R$ biologically inactive state.[11,12] The short-day plants will bloom when the $P_R$ concentration is higher than $P_{FR}$, and the longer-day plants need more daylight to flower.[13] Thus it is important for plants to be exposed to light, which has a suitable proportion of red and far-red light components.[8,14] Therefore, research on far-red phosphors is very meaningful for plant lighting in the agricultural field.

The phosphor-converted light-emitting diodes (LEDs), which show the advantages of energy-saving, long working lifetime, and environmental protection, have gained increasing attention as the next-generation light source.[15–23] In recent years, intense research efforts have been devoted into developing high-efficiency red phosphors for white LEDs, such as $NaMgGdTeO_6:Mn^{4+}$,[24] $Na_3MgZr(PO_4)_3:Eu^{3+}$,[25] $CaAl_{12}O_{19}:Mn^{4+}$,[26] and $LiCa_3MgV_3O_{12}:Eu^{3+}$.[27] In sharp contrast, there is little research on the far-red emitting phosphors for plant growth LEDs.[28–30] Thus, the research on the high-efficiency red phosphors for far-red LEDs used in plant cultivation has a far-reaching significance.

$Mn^{4+}$ ions can be doped into the octahedral sites in the host as an activator,[31,32] resulting in the efficient red or far-red emissions which are significant for plant growth.[33–37] $La_2LiSbO_6$ compound with double-perovskite structure, which contains two octahedral structures, [$SbO_6$] and [$LiO_6$], have be reported by M. L. López *et al.*[38] In this paper, $La_2LiSbO_6:Mn^{4+},Mg^{2+}$ (LLS:$Mn^{4+}$,$Mg^{2+}$) far-red-emitting phosphors have been systematically studied. Under the excitation of 338 nm, LLS:0.3%$Mn^{4+}$,1.6%$Mg^{2+}$ phosphors exhibited intense far-red emission around 712 nm ($^2E_g \rightarrow {}^4A_{2g}$ transition), which matched well with the absorption spectrum of phytochrome $P_{FR}$. Importantly, the internal quantum efficiency (IQE) of the LLS:0.3%$Mn^{4+}$,1.6%$Mg^{2+}$ phosphors reached as high as 92%. The temperature-dependent spectra illustrated that LLS:0.3% $Mn^{4+}$,1.6%$Mg^{2+}$ phosphors had excellent thermal stability with an activation energy of 0.12 eV, and the integral intensity at 423 K is 0.58-fold compared with its initial value at 303 K. All characteristics show that the LLS:$x$$Mn^{4+}$,$y$$Mg^{2+}$ far-red emitting phosphors would have potential application in plant growth LEDs.

*Key Lab of Advanced Transducers and Intelligent Control System, Ministry of Education and Shanxi Province, College of Physics and Optoelectronics, Taiyuan University of Technology, Taiyuan 030024, P. R. China. E-mail: huangxy04@126.com*

## Experimental section

LLS:$x$Mn$^{4+}$ ($x$ = 0.1–1.5%) phosphors were prepared by solid-state reaction method. The amount of final product was fixed at 0.005 mol for each sample. The starting materials of $Li_2CO_3$ (analytical reagent, AR), $Sb_2O_5$ (99%), $MnCO_3$ (AR) and $La_2O_3$ (99.99%) were weighed according to the molar ratio of 1.03 : (1 − $x$) : 2$x$ : 2 and ground in an agate mortar, then transferred to $Al_2O_3$ crucibles to pre-heat at 70 °C for 10 h in air. Then the obtained mixtures were ground thoroughly again, and calcined at 800 °C for 10 h in air. Subsequently, the obtained products were uniformly ground again and calcined at 1100 °C for 10 h in air to get the final samples. Finally, when the furnace was cooled down to room temperature, the obtained products were ground into fine powders for further characterizations. The LLS:0.3% Mn$^{4+}$,$y$Mg$^{2+}$ phosphors were prepared by using the similar method, and the MgO (AR) was weighed at 0.8%, 1.2%, 1.6%, and 2.0% of the total molar amount of Li atom.

The X-ray diffraction (XRD) patterns of the phosphors were measured by using a Bruker D8 ADVANCE diffractometer with Cu Kα radiation ($\lambda$ = 1.5406 Å). The morphology of the LLS:0.3% Mn$^{4+}$ phosphors was recorded by using a field-emission scanning electron microscope (FE-SEM; TESCAN MAIA3). The photoluminescence (PL) spectra/PL excitation (PLE) spectra were measured by an Edinburgh FS5 spectrometer with a 150 W continuous-wave xenon lamp as the excitation source. The temperature-dependent spectra were recorded on the same spectrometer equipping with a temperature controller. The luminescence decay curves and the IQE of the as-prepared sample were measured by Edinburgh FS5 spectrometer equipped with a pulsed xenon lamp as the excitation source and an integrating sphere coated with barium sulfate, respectively. The far-red light-emitting device was fabricated by coating the LLS:0.3%Mn$^{4+}$,1.6%Mg$^{2+}$ phosphors onto a 365 nm emitting InGaN chip, and the corresponding photoelectric properties of the device under a bias current of 300 mA were measured by using a spectroradiometer system (HAAS-2000, Everfine).

## Results and discussion

Fig. 1(a) shows the XRD patterns of LLS:$x$Mn$^{4+}$,$y$Mg$^{2+}$ ($x$ = 0.1%, 0.3%, 0.9% and 1.5%; $y$ = 0.8% and 1.6%) phosphors. All the diffraction peaks coincided well with the stand card of $La_2$-$LiNbO_6$ compound (JCPDS: 40-0895). Fig. 1(b) and (c) show the Rietveld refined results of LLS:0.3%Mn$^{4+}$ phosphors and the crystal structure of the LLS:0.3%Mn$^{4+}$ phosphors, respectively. From the Table 1 we could know that the LLS:0.3%Mn$^{4+}$ phosphors belong to double perovskite structure with monoclinic crystal system and $P121/n1$ space group. The LLS:0.3%Mn$^{4+}$ phosphors was build up with [$Sb0_6$], [$Li0_6$], and [$LaO_8$], in which [$Sb0_6$] and [$Li0_6$] (see Fig. 1(c)) were bound together by sharing the same oxygen atoms (sharing corners with each other).[38] The cell parameters of the LLS:0.3%Mn$^{4+}$ phosphors were: $a$ = 5.61710(8) Å, $b$ = 5.73188(8) Å, $c$ = 7.96305(11) Å, and $V$ = 256.380(8) Å$^3$. Considering the ion radii and coordination number (CN) of the Mn$^{4+}$ ions ($r$ = 0.53 Å, CN = 6),[39] Sb$^{5+}$ ions ($r$

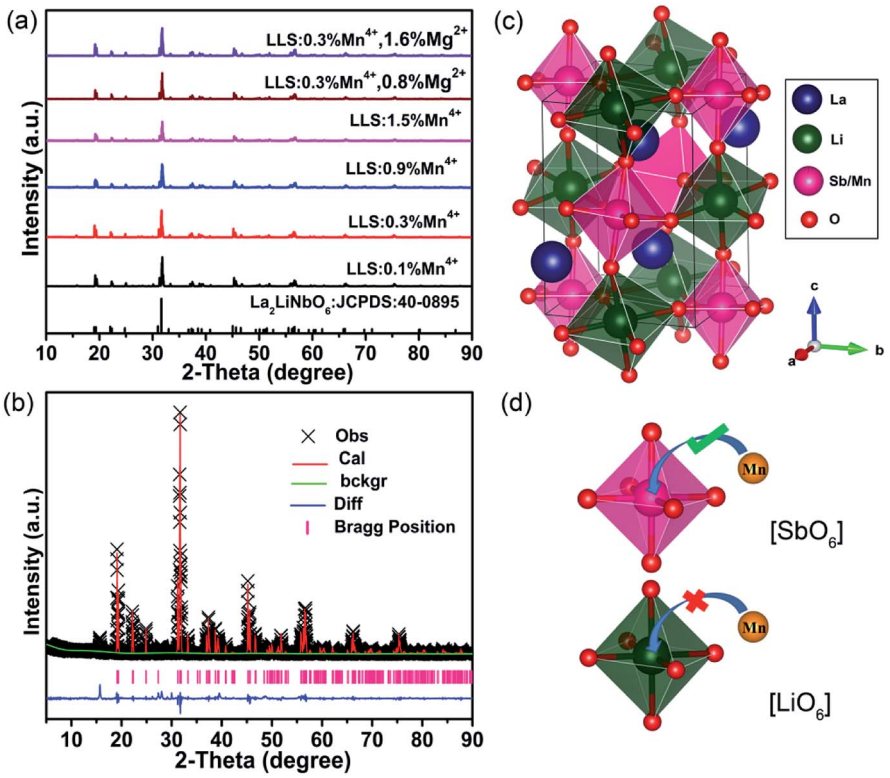


Fig. 1 (a) XRD patterns of the LLS:$x$Mn$^{4+}$,$y$Mg$^{2+}$ phosphors. (b) Rietveld refinement XRD pattern of the LLS:0.3%Mn$^{4+}$ phosphors. (c) The structure of the LLS:0.3%Mn$^{4+}$ phosphors. (d) The octahedron configuration diagrams of [$SbO_6$] and [$LiO_6$].

Table 1 Refined crystallographic parameters of LLS:0.3%$Mn^{4+}$ phosphors

| LLS:0.3%$Mn^{4+}$ | |
|---|---|
| Crystal system | Monoclinic |
| Space group | $P121/n1$ |
| Lattice parameters | $a = 5.61710(8)$ Å, $b = 5.73188(8)$ Å $c = 7.96305(11)$ Å, $\alpha = \gamma = 90°$ $\beta = 89.7464(10)°$ |
| Unit cell volume | $V = 256.380(8)$ Å$^3$ |

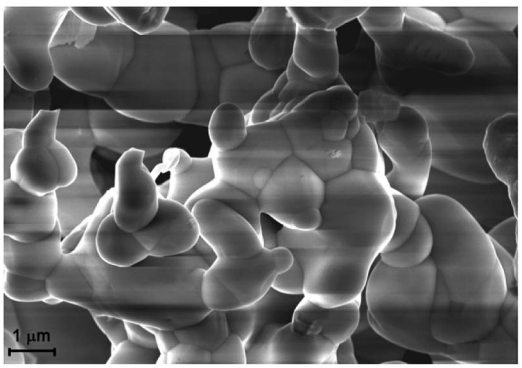


Fig. 2 A typical FE-SEM image of LLS:0.3%$Mn^{4+}$ phosphors.

= 0.6 Å, CN = 6),[40] and $Li^+$ ions ($r$ = 0.76 Å, CN = 6),[41] it was reasonable to conclude that the $Mn^{4+}$ ions would occupy the $Sb^{5+}$ sites in LLS host. Another parameter to determine which ions are substituted by $Mn^{4+}$ ions is the radii percentage difference ($D_r$) between the doping ions (here was $Mn^{4+}$ ions) and the possible substituted ions (here were $Sb^{5+}$ and $Li^+$ ions), and the ratio can be estimated by the following expression:[42,43]

$$D_r = \frac{R_m(CN) - R_d(CN)}{R_m(CN)} \times 100\% \quad (1)$$

where $R_m$(CN) and $R_d$(CN) are the ionic radii of the host cations and the doped ions, respectively. Herein, $R_d$(CN) = 0.53 Å and CN = 6 for $Mn^{4+}$ ions, $R_m$(CN) = 0.6 Å for $Sb^{5+}$ ions, and $R_m$(CN) = 0.76 Å for $Li^+$ ions. Thus, the $D_r$ of $Mn^{4+}$ ions substituted for $Sb^{5+}$ and $Li^+$ ions were 11.7% and 30.3%, respectively. Because the ratio of the $Mn^{4+}$ ions substituted for $Sb^{5+}$ ions was less than 30%, indicating in the LLS host the $Mn^{4+}$ ions were substitute for $Sb^{5+}$ sites to form the LLS:$x$$Mn^{4+}$ phosphors.[44] The typical FE-SEM image of the LLS:0.3%$Mn^{4+}$ phosphors shown in Fig. 2 indicated that the diameter of the irregular particles were about 0.5–4 μm.

Fig. 3(a) displays the PL ($\lambda_{ex}$ = 338 nm) and PLE ($\lambda_{em}$ = 712 nm) spectra of the LLS:0.3%$Mn^{4+}$ phosphors. Several excitation bands could be found in 220–580 nm wavelength range, and four characteristic peaks peaking at 273 nm (36 630 cm$^{-1}$; $Mn^{4+}$–$O^{2-}$ charge-transfer transition), 338 nm (29 586 cm$^{-1}$; $^4A_{2g} \rightarrow {}^4T_{1g}$ transition), 418 nm (23 923 cm$^{-1}$; $^4A_{2g} \rightarrow {}^2T_{2g}$ transition), and 481 nm (20 790 cm$^{-1}$; $^4A_{2g} \rightarrow {}^4T_{2g}$ transition) were obtained based on Gaussian functions.[45–47] Obviously, the excitation peak at 338 nm dominated the PLE spectrum. Under the excitation of 338 nm or 481 nm, the LLS:0.3%$Mn^{4+}$ phosphors exhibited a far-red emission band in 650–800 nm wavelength range peaking at 712 nm ($^2E_g \rightarrow {}^4A_{2g}$ transition).[24]

Fig. 3(b) presents the PL spectra of the LLS:$x$$Mn^{4+}$ ($x$ = 0.1–1.5%) phosphors. The maximum emission intensity reached when $x$ = 0.3%, indicating the existence of concentration quenching in LLS:$x$$Mn^{4+}$ phosphors. The critical distance ($R_c$) is a parameter for dopant ions in a particular lattice to determine whether exchange interaction or electric multipole interaction contribute to the concentration quenching, which can be obtained by the following formula:[48,49]

$$R_c = 2\left(\frac{3V}{4\pi x_c N}\right)^{1/3} \quad (2)$$

where $V$ is the volume of the unit cell and $N$ is the number of cation in the unit cell to be substituted by $Mn^{4+}$ ions; $x_c$ refers to the optimal doping content of $Mn^{4+}$ ions. Herein, $V$ = 256.380(8) Å$^3$, $N$ = 2, and $x_c$ = 0.3%. Thus, the value of $x_c$ was calculated to be 43.4 Å (>5 Å), indicating that it was electric multipole interaction contribute to the concentration quenching in LLS:$x$$Mn^{4+}$ phosphors.[50] Besides, the exact concentration quenching mechanism can be explored using the following formula expression:[51,52]

$$I/x = K[1 + \beta(x)^{\theta/3}]^{-1} \quad (3)$$

where $I$ and $x$ represent the PL intensity and doping concentration of $Mn^{4+}$ ions in LLS host, respectively; $\beta$ and $k$ are constants for specific host lattice; and $\theta$ = 6, 8, and 10 stands for electric dipole–dipole, dipole–quadrupole and quadrupole–quadrupole interaction, respectively.[53] Fig. 3(c) shows the relationship between log($x$) and log($I/x$). We could know that the slope of the fitting line was −1.52, thus $\theta$ = 4.56 which was close to 6, revealing that the quenching mechanism in LLS:$x$$Mn^{4+}$ phosphors is based on dipole–dipole interaction.

Fig. 3(d) depicts the luminescence decay curves of the $Mn^{4+}$ ions in the LLS:$x$$Mn^{4+}$ ($x$ = 0.1–1.5%) phosphors ($\lambda_{ex}$ = 338 nm; $\lambda_{em}$ = 712 nm). The decay curves of as-prepared samples could be well fitted by the following double exponential expression:[54–56]

$$I = A_1 \exp(-t/\tau_1) + A_2 \exp(-t/\tau_2) \quad (4)$$

herein, $I$ refer to the luminescent emission intensity at time $t$, and $A_1$ and $A_2$ are constants; $\tau_1$ and $\tau_2$ are the lifetimes for the exponential component; the decay lifetimes were found to be 2.079, 2.047, 1.997, 1.943, 1.821, and 1.741 ms for $x$ = 0.1%, 0.3%, 0.6%, 0.9%, 1.2%, and 1.5%, respectively. The decay lifetimes gradually decreased with the increasing $Mn^{4+}$ concentration, which can be attributed to the enhanced non-radiative energy transfer of $Mn^{4+}$ ions in LLS:$x$$Mn^{4+}$ phosphors.

To enhance the emission intensity and IQE of LLS:0.3%$Mn^{4+}$ phosphors, a series of $Mg^{2+}$ doped LLS:0.3%$Mn^{4+}$ phosphors had been synthesized. Fig. 4(a) and (b) shows the PL spectra of LLS:0.3%$Mn^{4+}$,$y$$Mg^{2+}$ phosphors doped with different $Mn^{4+}$ concentrations and the corresponding relative intensity as a function of $Mg^{2+}$ concentration, respectively. Clearly, the

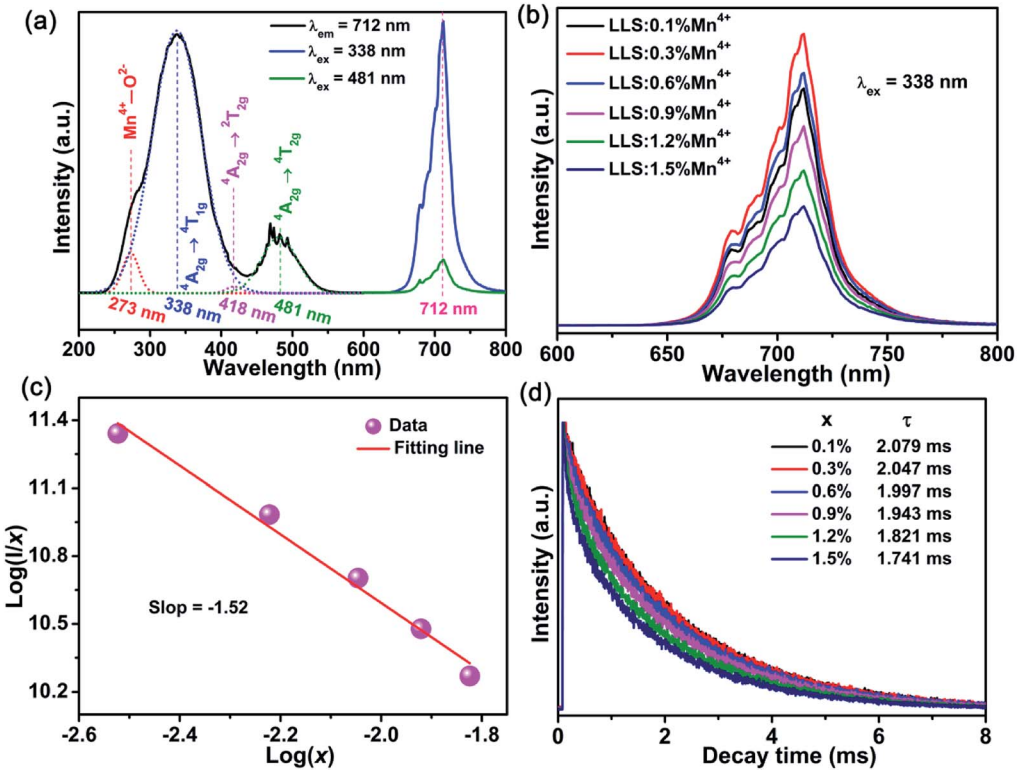


Fig. 3 (a) The PLE and PL spectra of LLS:0.3%$Mn^{4+}$ phosphors. (b) The PL spectra of LLS:x$Mn^{4+}$ ($x$ = 0.1–1.5%) phosphors. (c) Plot of log($I$/$x$) *vs.* log($x$) of $Mn^{4+}$ ions in LLS:x$Mn^{4+}$ phosphors excited at 338 nm. (d) The luminescence decay curves of LLS:x$Mn^{4+}$ ($x$ = 0.1–1.5%) phosphors ($\lambda_{ex}$ = 338 nm; $\lambda_{em}$ = 712 nm).

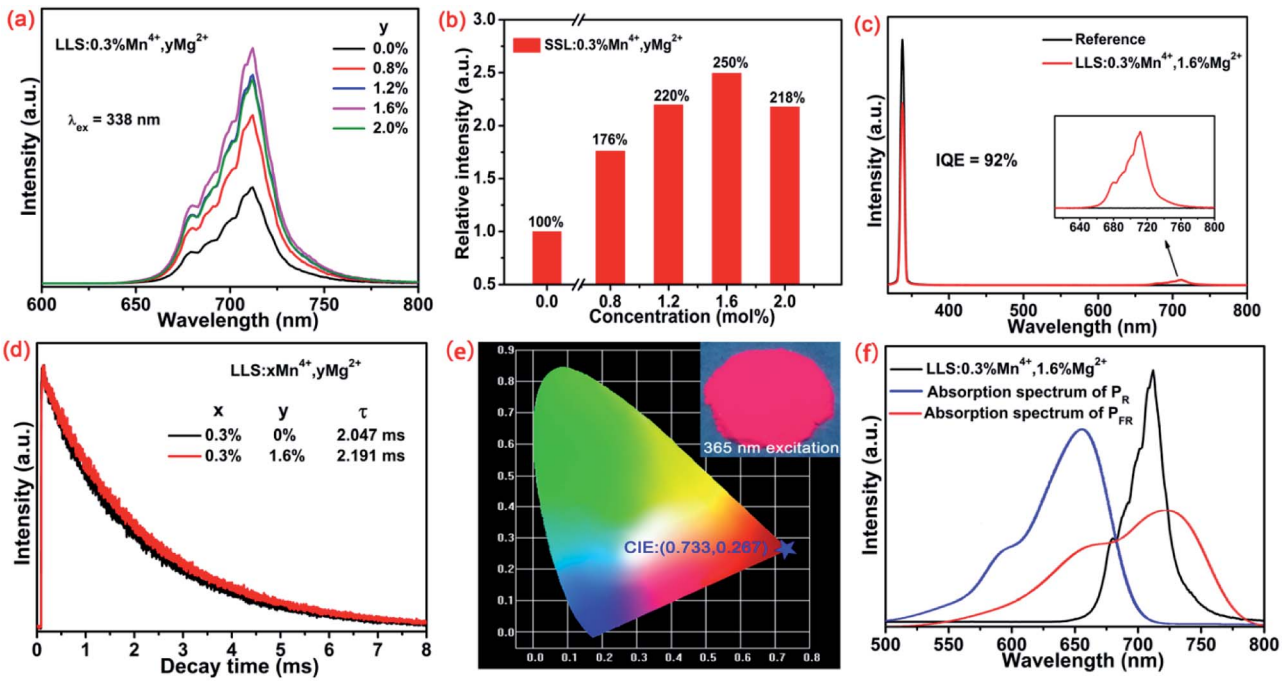


Fig. 4 (a) PL spectra of the LLS:0.3%$Mn^{4+}$,y$Mg^{2+}$ phosphors excited at 338 nm. (b) The relative intensity as a function of $Mg^{2+}$ concentration. (c) The excitation profile of the reference $BaSO_4$ and the emission spectrum of the LLS:0.3%$Mn^{4+}$,1.6%$Mg^{2+}$ phosphors at 338 nm excitation. (d) Decay curves of the LLS:0.3%$Mn^{4+}$,y$Mg^{2+}$ ($y$ = 0% and 1.6%) phosphors. (e) CIE chromaticity diagram of the LLS:0.3%$Mn^{4+}$,1.6%$Mg^{2+}$ phosphors. (f) PL spectrum of LLS:0.3%$Mn^{4+}$,1.6%$Mg^{2+}$ phosphors together with the absorption spectra of phytochrome $P_R$ and $P_{FR}$.

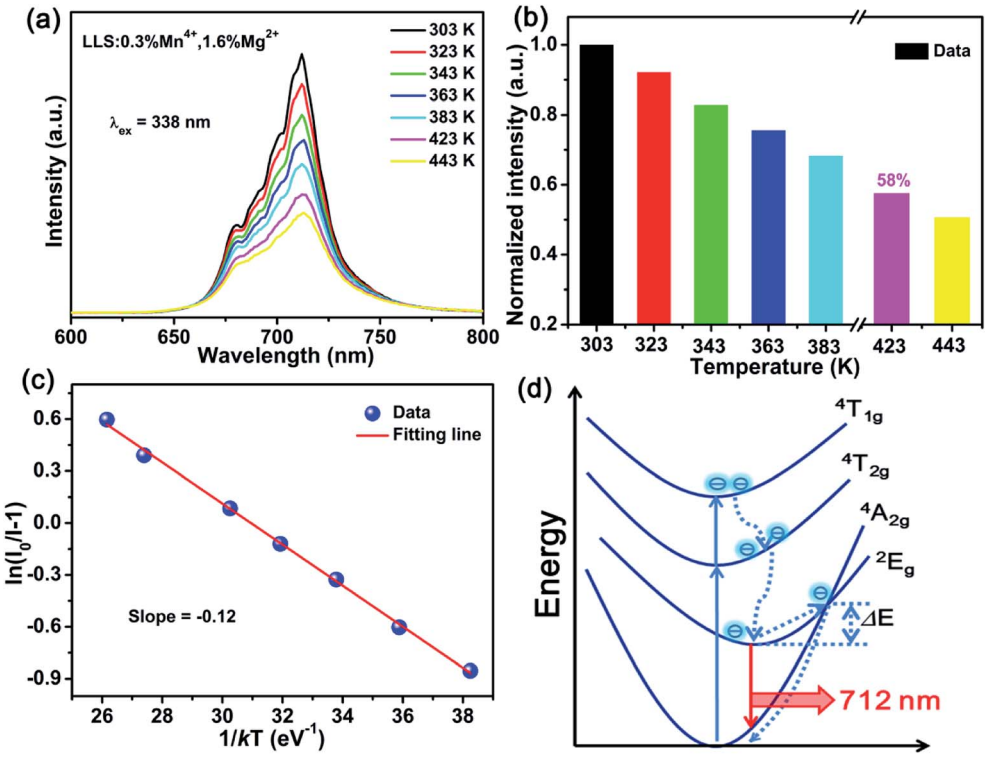


Fig. 5 (a) Temperature-dependent spectra of LLS:0.3%$Mn^{4+}$,1.6%$Mg^{2+}$ phosphors. (b) Normalized intensity as a function of temperature. (c) Plots of $1/kT$ *vs.* ln ($I_0/I - 1$) for the LLS:0.3%$Mn^{4+}$,1.6%$Mg^{2+}$ phosphors. (d) Configuration coordinate diagram of $^4A_{2g}$, $^4T_{1g}$, $^4T_{2g}$, and $^2E_g$ levels in the octahedron.

emission intensity of LLS:0.3%$Mn^{4+}$ phosphors was enhanced by the introduction of $Mg^{2+}$ ions. Importantly, the emission intensity of the LLS:0.3%$Mn^{4+}$,1.6%$Mg^{2+}$ phosphors was about 2.5-fold of the LLS:0.3%$Mn^{4+}$ counterpart. In the LLS:0.3% $Mn^{4+}$,1.6%$Mg^{2+}$ phosphors, the doped $Mg^{2+}$ ions was served as the charge compensator. Because the radii of the $Mg^{2+}$ ions ($r$ = 0.72 nm, CN = 6) and $Li^+$ ions ($r$ = 0.76 Å, CN = 6) are relatively close, so the $Mg^{2+}$ ions might substitute for $Li^+$ sites or occupy $Li^+$ vacancies, and then compensate the imbalanced charges in LLS:0.3%$Mn^{4+}$ phosphors.[57] As a result of charge compensation, the formation of the defects which served as quenching centers in the LLS:0.3%$Mn^{4+}$ phosphors was avoided. Thus, the emission intensity and IQE of the LLS:0.3%$Mn^{4+}$ phosphors were largely improved. Meanwhile, the IQE of the LLS:0.3%$Mn^{4+}$ had also been largely improved by $Mg^{2+}$ co-doping. The IQEs of LLS:0.3%$Mn^{4+}$ and LLS:0.3%$Mn^{4+}$,1.6%$Mg^{2+}$ (see Fig. 4(c)) were measured to be 61% and 92%, respectively, which was higher than that of $K_2NaAlF_6$:$Mn^{4+}$ (IQE = 58.4%), $Ba_2TiGe_2O_8$:$Mn^{4+}$ (IQE = 35.6%), and $Mg_7Ga_2GeO_{12}$:$Mn^{4+}$ (IQE = 28.13%).[58–60] The decay lifetime of the LLS:0.3%$Mn^{4+}$,1.6%$Mg^{2+}$ phosphors was longer than that of LLS:0.3%$Mn^{4+}$ counterpart (see Fig. 4(d)). In addition, the CIE coordinates of LLS:0.3%$Mn^{4+}$,1.6%$Mg^{2+}$ phosphors were (0.733, 0.267), locating in the far-red region. Importantly, as shown in Fig. 4(f), the PL spectrum of the LLS:0.3%$Mn^{4+}$,1.6%$Mg^{2+}$ phosphors matched well with the absorption spectrum of $P_{FR}$, which indicated the LLS:0.3% $Mn^{4+}$,1.6%$Mg^{2+}$ phosphors had great potential to be used as far-red emitting materials in LEDs for plant growth application.

Fig. 5(a) shows the temperature-dependent spectra of the LLS:0.3%$Mn^{4+}$,1.6%$Mg^{2+}$ phosphors. The profiles of the emission spectra were almost the same, but the emission intensity gradually reduced with the increasing temperature. As shown in Fig. 5(b), the emission intensity of the LLS:0.3%$Mn^{4+}$,1.6%$Mg^{2+}$ phosphors at 423 K remained about 58% compared that at 303 K, which was better than that of $Ca_3La_2W_2O_{12}$:$Mn^{4+}$ (29%), $CaLaMgNbO_6$:$Mn^{4+}$ (45%), $SrLaScO_4$:$Mn^{4+}$ (15%), and $Gd_2$-$ZnTiO_6$:$Mn^{4+}$ (27.2%),[61–64] indicating that the LLS:0.3% $Mn^{4+}$,1.6%$Mg^{2+}$ phosphors had good thermal stability. The corresponding activation energy can be obtained by using the following expression:[65,66]

$$I(T) = I_0\left[1 + c\exp\left(-\frac{\Delta E}{kT}\right)\right]^{-1} \quad (5)$$

where $I(T)$ and $I_0$ are the intensity at temperature $T$ and the initial intensity, respectively; $k$ is the Boltzmann constant and $c$ is a constant. The activation energy of the LLS:0.3%$Mn^{4+}$,1.6% $Mg^{2+}$ phosphors, which was obtained from the fitting result in Fig. 5(c), was 0.12 eV. The possible thermal quenching behavior of the LLS:0.3%$Mn^{4+}$,1.6%$Mg^{2+}$ phosphors can be explained by a simple configuration coordinate diagram of $^4A_{2g}$, $^4T_{1g}$, $^4T_{2g}$, and $^2Eg$ levels, as shown in Fig. 5(d). At room temperature, the electrons on the ground state $^4A_{2g}$ were excited to the excited state under the excitation of 338 nm or 481 nm, and then return to the lowest excited state $^2E_g$ by nonradiative transition. Eventually, the electrons on the $^2E_g$ level return to $^4A_{2g}$ level with the emission of far-red light (the red line). But when the

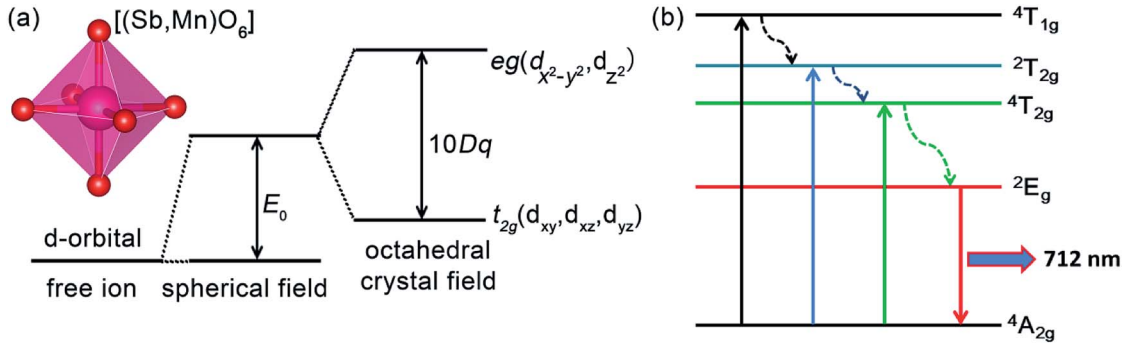


Fig. 6 (a) The simple schematic diagram of the d-orbital splitting in octahedral crystal field with octahedral structure of $[(Sb,Mn)O_6]$. (b) A simple schematic diagram of $Mn^{4+}$ ions energy level.

temperature increased, the electrons on the $^2E_g$ level are more likely to get enough energy to reach the crossover point of the states of $^4A_{2g}$ and $^2E_g$, then return to the ground state by non-radiative relaxation with no light emission,[39,67] which result in the decrease of the emission intensity of the LLS:0.3% $Mn^{4+}$,1.6%$Mg^{2+}$ phosphors.

In this host, the $Mn^{4+}$ ions were in a strong field environment, which can be reflected by the ratio of crystal filed strength (Dq) to Racah parameter $B$. The corresponding Dq and $B$ can be determined by the following eqn (6) and (7):[68]

$$\mathrm{Dq} = E(^4A_{2g} - {}^4T_{2g})/10 \quad (6)$$

$$\frac{\mathrm{Dq}}{B} = \frac{15(x-8)}{(x^2-10x)} \quad (7)$$

where $x$ is defined as:

$$x = \frac{E(^4A_{2g} \rightarrow {}^4T_{1g}) - E(^4A_{2g} \rightarrow {}^4T_{2g})}{\mathrm{Dq}} \quad (8)$$

And according to the fitting result of PL spectrum of the LLS:0.3%$Mn^{4+}$ phosphors, the peaking energy of $^2E_g \rightarrow {}^4A_{2g}$ transition was about 14 045 $cm^{-1}$. Therefore, the Racah parameter $C$ can be calculated as following:[69,70]

$$\frac{E(^2E_g \rightarrow {}^4A_{2g})}{B} = \frac{3.05C}{B} + 7.9 - \frac{1.8B}{\mathrm{Dq}} \quad (9)$$

Thus, based on the eqn (6)–(9), the values of crystal parameter Dq, $B$, and $C$ was 2079, 898, 2509 $cm^{-1}$, respectively. Meanwhile, the value of the Dq/$B$ is about 2.32, indicating the $Mn^{4+}$ ions were in a strong field environment in the LLS host. In a strong octahedral filed environment (surrounded by six oxygen atoms), as shown in Fig. 6(a), the original degenerate 3d orbitals of free $Mn^{4+}$ ions, which are $d_{x^2} - d_{y^2}$, $d_{z^2}$, $d_{xy}$, $d_{yz}$, and $d_{xz}$, spilt into two degenerate and three degenerate. The energy of the two degenerate consisting of $d_{x^2} - d_{y^2}$ and $d_{z^2}$, is higher than that of the three degenerate consisting of $d_{xy}$, $d_{yz}$, and $d_{xz}$.[13] Fig. 6(b) also gives the simple schematic diagram of $Mn^{4+}$ ions energy level in strong octahedral filed environment. The possible transitions between different levels can be expressed as the following process. Under the excitation of 338 nm or 481 nm, the electrons on the ground state $^4A_{2g}$ were excited to the excited levels, and then relaxed the lowest excited level $^2E_g$. Finally, the far-red light peaking at 712 nm was emitted with the electrons on the $^2E_g$ level return to the $^4A_{2g}$ level.

A prototype far-red emitting LED device was fabricated by coating the as-prepared LLS:0.3%$Mn^{4+}$,1.6%$Mg^{2+}$ phosphors on a 365 nm near-UV LED chip, and Fig. 7 displays the corresponding electroluminescence (EL) spectrum of the prototype LED device under a bias current of 300 mA. An intense far-red emission band in the wavelength rang of 650–780 nm ($^2E_g \rightarrow {}^4A_{2g}$ transition) was observed and the far-red light around the device could be seen clearly by comparing the inset (i) and (ii) in Fig. 7. All the results indicate the LLS:0.3%$Mn^{4+}$,1.6%$Mg^{2+}$ phosphors have a promising prospect in the plant lighting field.

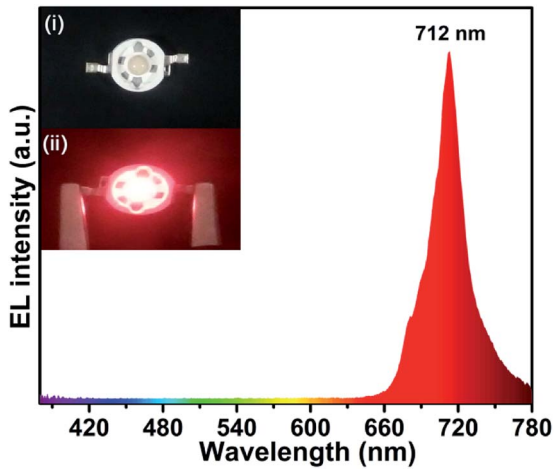


Fig. 7 The EL spectrum of the as-prepared far-red-emitting LED device. Insets show the digital photographs of (i) the fabricated LED device and (ii) the working device under 300 mA driven.

## Conclusions

In conclusion, double perovskite LLS:$Mn^{4+}$,$Mg^{2+}$ far-red emitting phosphors with high IQE and excellent thermal stability were synthesized by traditional solid-state reaction method. The optimal doping concentration of $Mn^{4+}$ and $Mg^{2+}$ ions in

LLS:$Mn^{4+}$,$Mg^{2+}$ phosphors were 0.3% and 1.6%, respectively. Under the excitation of 338 nm, the LLS:0.3%$Mn^{4+}$,1.6%$Mg^{2+}$ phosphors showed an intense far-red-emitting band peaking at 712 nm and the emission intensity at 423 K remained 58% of its initial value at 303 K. By doping $Mg^{2+}$ ions in LLS:0.3%$Mn^{4+}$ phosphors, the luminescence intensity of $Mn^{4+}$ ions was enhanced by 2.5-fold and the corresponding IQE was also improved from 61% to 92%. Remarkably, the emission spectrum of the LLS:0.3%$Mn^{4+}$,1.6%$Mg^{2+}$ phosphors could match well with the absorption spectrum of the phytochrome $P_{FR}$. All the outstanding properties of the double perovskite LLS:$Mn^{4+}$,$Mg^{2+}$ phosphors make it be a promising far-red-emitting phosphor for applications in plant growth LEDs.

## Conflicts of interest

There are no conflicts to declare.

## Acknowledgements

This work was supported by the National Natural Science Foundation of China (No. 51502190), the Program for the Outstanding Innovative Teams of Higher Learning Institutions of Shanxi, and the Open Fund of the State Key Laboratory of Luminescent Materials and Devices (South China University of Technology, No. 2017-skllmd-01)

## Notes and references

1 N. Yeh and J.-P. Chung, *Renewable Sustainable Energy Rev.*, 2009, **13**, 2175–2180.
2 X. Huang, *J. Alloys Compd.*, 2017, **690**, 356–359.
3 P. Du, X. Huang and J. S. Yu, *Chem. Eng. J.*, 2018, **337**, 91–100.
4 C. C. Lin, A. Meijerink and R. S. Liu, *J. Phys. Chem. Lett.*, 2016, **7**, 495–503.
5 D. Wu, W. Xiao, L. Zhang, X. Zhang, Z. Hao, G.-H. Pan, Y. Luo and J. Zhang, *J. Mater. Chem. C*, 2017, **5**, 11910–11919.
6 K. Li, H. Lian, Y. Han, M. Shang, R. Van Deun and J. Lin, *Dyes Pigm.*, 2017, **139**, 701–707.
7 B. Li and X. Huang, *Ceram. Int.*, 2018, **44**, 4915–4923.
8 R. Cao, Z. Shi, G. Quan, Z. Luo, P. Tang, H. Ao and X. Yu, *Opt. Mater.*, 2016, **57**, 212–216.
9 J. Long, X. Yuan, C. Ma, M. Du, X. Ma, Z. Wen, R. Ma, Y. Wang and Y. Cao, *RSC Adv.*, 2018, **8**, 1469–1476.
10 T. Nakajima and T. Tsuchiya, *ACS Appl. Mater. Interfaces*, 2015, **7**, 21398–21407.
11 G. D. Massa, *HortScience*, 2008, **43**, 1951–1956.
12 H. Smith, *Nature*, 2000, **407**, 585–591.
13 Z. Zhou, J. Zheng, R. Shi, N. Zhang, J. Chen, R. Zhang, H. Suo, E. M. Goldys and C. Guo, *ACS Appl. Mater. Interfaces*, 2017, **9**, 6177–6185.
14 J. Chen, N. Zhang, C. Guo, F. Pan, X. Zhou, H. Suo, X. Zhao and E. M. Goldys, *ACS Appl. Mater. Interfaces*, 2016, **8**, 20856–20864.
15 X. Huang, S. Wang, B. Li, Q. Sun and H. Guo, *Opt. Lett.*, 2018, **43**, 1307–1310.
16 X. Huang, *Nat. Photonics*, 2014, **8**, 748–749.
17 P. Du, X. Huang and J. S. Yu, *Inorg. Chem. Front.*, 2017, **4**, 1987–1995.
18 B. Li, X. Huang, H. Guo and Y. Zeng, *Dyes Pigm.*, 2018, **150**, 67–72.
19 P. Du, L. Luo, X. Huang and J. S. Yu, *J. Colloid Interface Sci.*, 2018, **514**, 172–181.
20 X. Huang, B. Li and H. Guo, *J. Alloys Compd.*, 2017, **695**, 2773–2780.
21 X. Huang, H. Guo and B. Li, *J. Alloys Compd.*, 2017, **720**, 29–38.
22 T. Senden, E. J. van Harten and A. Meijerink, *J. Lumin.*, 2018, **194**, 131–138.
23 T. Sasaki, J. Fukushima, Y. Hayashi and H. Takizawa, *J. Lumin.*, 2018, **194**, 446–451.
24 K. Li, H. Lian and R. V. Deun, *J. Lumin.*, 2018, **198**, 155–162.
25 G. Zhu, Z. Li, C. Wang, F. Zhou, Y. Shi, Y. Wen and S. Xin, *J. Mater. Sci.: Mater. Electron.*, 2017, **29**, 2216–2221.
26 T. Murata, T. Tanoue, M. Iwasaki, K. Morinaga and T. Hase, *J. Lumin.*, 2005, **114**, 207–212.
27 X. Huang and H. Guo, *Dyes Pigm.*, 2018, **154**, 82–86.
28 R. Cao, Z. Shi, G. Quan, T. Chen, S. Guo, Z. Hu and P. Liu, *J. Lumin.*, 2017, **188**, 577–581.
29 Q. Sun, S. Wang, B. Li, H. Guo and X. Huang, *J. Lumin.*, 2018, **203**, 371–375.
30 X. Huang, J. Liang, B. Li, L. Sun and J. Lin, *Opt. Lett.*, 2018, **43**, 3305–3308.
31 M. G. Brik and A. M. Srivastava, *ECS J. Solid State Sci. Technol.*, 2013, **2**, R148–R152.
32 X. Zhang, J. Nie, S. Liu, Y. Li and J. Qiu, *J. Am. Ceram. Soc.*, 2017, **00**, 1–9.
33 S. Wang, Q. Sun, B. Devakumar, L. Sun, J. Liang and X. Huang, *RSC Adv.*, 2018, **8**, 30191–30200.
34 K. Sankarasubramanian, B. Devakumar, G. Annadurai, L. Sun, Y.-J. Zeng and X. Huang, *RSC Adv.*, 2018, **8**, 30223–30229.
35 Y. Li, S. Qi, P. Li and Z. Wang, *RSC Adv.*, 2017, **7**, 38318–38334.
36 J. Liang, L. Sun, B. Devakumar, S. Wang, Q. Sun, H. Guo, B. Li and X. Huang, *RSC Adv.*, 2018, **8**, 27144–27151.
37 Q. Sun, S. Wang, B. Devakumar, B. Li, L. Sun, L. Jia and H. Xiaoyong, *RSC Adv.*, 2018, **8**, 28538–28545.
38 M. L. López, M. L. Veiga, J. Rodríguez-Carvajal, F. Fernández, A. Jerez and C. Pico, *Mater. Res. Bull.*, 1992, **27**, 647–654.
39 C. Yang, Z. Zhang, G. Hu, R. Cao, X. Liang and W. Xiang, *J. Alloys Compd.*, 2017, **694**, 1201–1208.
40 J. Zhong, S. Zhou, D. Chen, J. Li, Y. Zhu, X. Li, L. Chen and Z. Ji, *Dalton Trans.*, 2018, **47**, 8248.
41 J. Zhong, D. Chen, X. Chen, K. Wang, X. Li, Y. Zhu and Z. Ji, *Dalton Trans.*, 2018, **47**, 6528–6537.
42 K. Li, H. Lian, M. Shang and J. Lin, *Dalton Trans.*, 2015, **44**, 20542–20550.
43 C. Yue, W. Wang, Q. Wang and Y. Jin, *J. Alloys Compd.*, 2016, **683**, 575–578.
44 S. G. Prasanna Kumar, R. Hari Krishna, N. Kottam, P. Krishna Murthy, C. Manjunatha, R. Preetham, C. Shivakumara and T. Thomas, *Dyes Pigm.*, 2018, **150**, 306–314.

45 M. H. Du, *J. Mater. Chem. C*, 2014, **2**, 2475–2481.
46 Z. Lu, H. Wang, D. Yu, T. Huang, L. Wen, M. Huang, L. Zhou and Q. Wang, *Opt. Laser Technol.*, 2018, **108**, 116–123.
47 Z. Lu, T. Huang, R. Deng, H. Wang, L. Wen, M. Huang, L. Zhou and C. Yao, *Superlattices Microstruct.*, 2018, **117**, 476–487.
48 H. Guo, X. Huang and Y. Zeng, *J. Alloys Compd.*, 2018, **741**, 300–306.
49 S. Zhang, Y. Hu, H. Duan, Y. Fu and M. He, *J. Alloys Compd.*, 2017, **693**, 315–325.
50 K. Li, H. Lian and R. Van Deun, *Dalton Trans.*, 2018, **47**, 2501–2505.
51 L. Jing, X. Liu and Y. Li, *J. Lumin.*, 2015, **158**, 351–355.
52 A. Fu, L. Zhou, S. Wang and Y. Li, *Dyes Pigm.*, 2018, **148**, 9–15.
53 B. Ma and B. Liu, *J. Lumin.*, 2017, **188**, 54–59.
54 X. Wu, Y. Jiao, O. Hai, Q. Ren, F. Lin and H. Li, *J. Alloys Compd.*, 2018, **730**, 521–527.
55 A. Guan, P. Chen, L. Zhou, G. Wang, X. Zhang and J. Tang, *Spectrochim. Acta, Part A*, 2017, **173**, 53–58.
56 P. Ma, Y. Song, B. Yuan, Y. Sheng, C. Xu, H. Zou and K. Zheng, *Ceram. Int.*, 2017, **43**, 60–70.
57 L. Wang, L. Yuan, Y. Xu, R. Zhou, B. Qu, N. Ding, M. Shi, B. Zhang, Y. Chen, Y. Jiang, D. Wang and J. Shi, *Appl. Phys. A*, 2014, **117**, 1777–1783.
58 C. Wu, J. Li, H. Xu, J. Wu, J. Zhang, Z. Ci, L. Feng, C. Cao, Z. Zhang and Y. Wang, *J. Alloys Compd.*, 2015, **646**, 734–740.
59 L. Y. Wang, E. H. Song, T. T. Deng, Y. Y. Zhou, Z. F. Liao, W. R. Zhao, B. Zhou and Q. Y. Zhang, *Dalton Trans.*, 2017, **46**, 9925–9933.
60 R. Cao, Y. Ye, Q. Peng, G. Zheng, H. Ao, J. Fu, Y. Guo and B. Guo, *Dyes Pigm.*, 2017, **146**, 14–19.
61 X. Huang and H. Guo, *Dyes Pigm.*, 2018, **152**, 36–42.
62 H. Chen, H. Lin, Q. Huang, F. Huang, J. Xu, B. Wang, Z. Lin, J. Zhou and Y. Wang, *J. Mater. Chem. C*, 2016, **4**, 2374–2381.
63 U. B. Humayoun, S. N. Tiruneh and D.-H. Yoon, *Dyes Pigm.*, 2018, **152**, 127–130.
64 G. Jiang, B. Yang, G. Zhao, Y. Liu, J. Zou, H. Sun, H. Ou, Y. Fang and J. Hou, *Opt. Mater.*, 2018, **83**, 93–98.
65 X. Huang, B. Li, H. Guo and D. Chen, *Dyes Pigm.*, 2017, **143**, 86–94.
66 Q. Peng, R. Cao, Y. Ye, S. Guo, Z. Hu, T. Chen and G. Zheng, *J. Alloys Compd.*, 2017, **725**, 139–144.
67 S. Zhang and Y. Hu, *J. Lumin.*, 2016, **177**, 394–401.
68 L. Qin, S. Bi, P. Cai, C. Chen, J. Wang, S. I. Kim, Y. Huang and H. J. Seo, *J. Alloys Compd.*, 2018, **755**, 61–66.
69 R. Cao, X. Liu, K. Bai, T. Chen, S. Guo, Z. Hu, F. Xiao and Z. Luo, *J. Lumin.*, 2018, **197**, 169–174.
70 P. Cai, L. Qin, C. Chen, J. Wang, S. Bi, S. I. Kim, Y. Huang and H. J. Seo, *Inorg. Chem.*, 2018, **57**, 3073–3081.